Independent Component Analysis (ICA) Based Method for Estimating the Deformation of Highways in Permafrost Region (HPICA)—A Case Study of Maduo Section of Gongyu Highway

Xuemin Xing, Jiawang Ge, Wei Peng, Jun Zhu, Bin Liu, Jiancun Shi, and Guanfeng Zheng

***Abstract*—Highways built in permafrost regions are susceptible to deformations and instability of the roadbed caused by climatic factors. Long-term deformation monitoring is essential to reveal the freeze-thaw-related deformations. When using Interferometric Synthetic Aperture Radar (InSAR) for permafrost highway monitoring, the majority of different physical phase components are usually considered as equally weighted, and the permafrost deformation-related components are mostly modeled with an empirical mathematical model. This may induce uncertainty and difficulties to remove the atmospheric delay and orbital error, which affects both the accuracy and efficiency of deformation estimation. To address these limitations, we propose an independent component analysis (ICA) based method for estimating the deformation of highways in permafrost regions (HPICA). In HPICA, the Fast ICA is utilized to separate the original InSAR unwrapped phases, and then the extracted freeze-thaw deformation-related components are modeled considering the climatic factors. The simulated experiments show that the spatial ICA can more accurately separate the deformation-related signals from the mixed signals than that of temporal ICA. The Maduo section of Gongyu Highway on the Tibetan Plateau was selected as a study area in the real-data experiment. The results showed the maximum cumulative settlement spanning January 2020 to January 2022 was up to –140.8 mm. A comparative analysis indicated that the modeling accuracy of HPICA is with significant improvement. Besides, HPICA could reveal the boundaries of different permafrost regions according to the nature of permafrost, thus assisting in spatial classification of different types of soil regions.**

***Index Terms*—Deformation estimation, Gongyu Highway, independent component analysis (ICA), Interferometric Synthetic Aperture Radar (InSAR), permafrost.**

Manuscript received 19 September 2023; revised 5 November 2023; accepted 13 November 2023. Date of publication 4 December 2023; date of current version 6 December 2023. This work was supported in part by the National Natural Science Foundation of China under Grant 42074033, Grant 42204046, Grant 41904003, Grant 41701536, and Grant 61701047, in part by the Natural Science Foundation of Hunan Province under Grant 2022JJ30589 and Grant 2022JJ40472, in part by the Research Foundation of the Department of Natural Resources of Hunan Province under Grant 20230118CH, in part by the Department of Traffic Transportation of Hunan Province under Grant 202211, in part by the Changsha Innovation Talent Promotion Plan Project for Distinguished Young Scholar under Grant kq2209011, and in part by the Changsha University of Science and Technology Graduate Student Research Innovation Program under Grant CXCLY2022009. *(Corresponding author: Wei Peng.)*

Xuemin Xing, Jiawang Ge, Wei Peng, Jun Zhu, Bin Liu, Jiancun Shi, and Guanfeng Zheng are with the School of Traffic and Transportation Engineering, Changsha University of Science and Technology, Changsha 410114, China, and also with the Institute of Radar Remote Sensing Applications for Traffic Surveying and Mapping, Changsha University of Science and Technology, Changsha 410114, China (e-mail: xuemin.xing@csust.edu.cn; gjw@stu.csust.edu.cn; pengwei@csust.edu.cn; jzhu@csust.edu.cn; binliu@csust.edu.cn; jc.shi@csust.edu.cn; 21201050156@stu.csust.edu.cn).

Digital Object Identifier 10.1109/JSTARS.2023.3336916

I. Introduction

PERMAFROST regions in China exhibit a broad distribution, encompassing both seasonal and continuous types, covering approximately one-half and one-fourth of the total land area in the nation, respectively [1]. Due to its high temperature sensitivity [2], [3], [4], highways built in those permafrost regions are susceptible to roadbed instability caused by external environmental-related deformation. Therefore, it is of great significance to undertake long-term, large-scale monitoring of highway deformation in permafrost regions. Multitemporal Interferometric Synthetic Aperture Radar (MT-InSAR) has demonstrated distinct advantages over the traditional InSAR method, achieving extensive applications and valuable results in monitoring the deformation of highways in permafrost regions [5], [6], [7], [8], [9]. For example, Chen et al. [10] used SBAS-InSAR technique to analyze the time-series deformation of a permafrost region in the southern Tibetan Plateau. Li et al. [11] utilized an improved time-series InSAR technique to acquire the surface deformation outcomes for the Heihe permafrost region (Heilongjiang Province, China) and unveiled the accelerated degradation features of island permafrost at escalating temperatures. Most of the traditional MT-InSAR techniques treated the unwrapped phase components (elevation residuals, orbital correlation components, deformation components, etc.) as equal-weighted. Meanwhile, they assumed the deformation correlation components using the mathematical empirical model, and then separated the residual high-pass (HP) deformation components employing the spatio–temporal filtering method [12], [13], [14]. However, these approaches involved an artificial assumption of equal weighting among the components, leading to uncertainties and excessive residual phases, which induced significant errors in deformation parameter calculation or even unsolvable phenomenon. Meanwhile, there are increasing challenges for the removal of atmospheric delays and orbital errors from the original phases solely through spatiotemporal filtering of the residual phase. Furthermore, the failure to account for the physical attributes of deformation when modeling permafrost-related

deformation components makes the empirical model difficult to capture the rational temporal evolution of permafrost deformation adequately, significantly reducing the accuracy of deformation estimation.

As a blind source separation technique, independent component analysis (ICA) can separate the original signal into independent components without requiring prior information. In this way, it offers the foundation for the physical interpretation of the deformation signal and extraction of the corresponding physical parameters [15], [16], [17], [18], [19], [20], [21]. Scholars have attempted to apply the ICA technique in assisting the InSAR phase separation. For instance, Gaddes et al. used the ICA method to isolate the deformation of the Ecuadorian volcano from InSAR measurements. The authors proved the ICA method's capability in processing InSAR data, effectively segregating deformation component signal caused by a volcanic eruption [22]. Zhu et al. used ICA to separate the InSAR time-series signals from the Santa Ana Basin, revealing two different spatial and temporal deformation patterns in the basin. Moreover, they effectively extracted the seasonal deformation components related to groundwater changes and the long-term components with large-scale spatial patterns [23]. Peng et al. applied ICA to the time-series deformation of the Wilcox Basin and succeeded in separating a set of independent signals. Their results not only revealed two different spatial and temporal deformation features in the basin but also filtered the residuals of the signals, thus enhancing the deformation time-series [24]. Given that the physical properties of deformation were not introduced in the empirical model, Xing et al. physically modeled the deformation of soft soil area at the Beijing Airport based on Poisson curves. Their ultimate objective was to improve the deformation estimation accuracy and analyze the causes of soft soil settlement [16]. In addition, some scholars have focused on the physical modeling of permafrost deformation and achieved excellent outcomes. The basic idea is to incorporate the physical coefficients that affect the deformation of permafrost into the model, including the thawing coefficient of permafrost, the freezing coefficient, and the key climatic factors, such as temperature and precipitation [11], [25], [26], [27], [28], [29], [30].

This article proposes an ICA-based method for time-series InSAR deformation estimation for highways in permafrost regions, namely HPICA. First, the spatial ICA (sICA) technique was utilized to separate the InSAR temporal phase signals. The statistically independent components of the permafrost deformation phase were obtained based on the spatial and temporal distribution characteristics of permafrost with the influence of the climatic environment. Second, the components related to the permafrost deformation and the main climatic factors were physically modeled, respectively. Accordingly, the system of phase equations was developed to estimate the physical parameters in the model, and then the time-series deformations of the permafrost regions were generated and analyzed in reverse to reveal the characteristics of the freeze-thaw deformation. HPICA extracts the permafrost-related phase signals from the unwrapped phases, enabling modeling based on the extracted corresponding phase components, which can ignore the uncertainty of assuming equal weighted modeling in InSAR, and improve the deformation modeling accuracy.

II. Methodology

A. InSAR Signal Separation Based on Fast Independent Component Analysis (FastICA)

Suppose $N+1$ SAR images of the same region are acquired, M differential interferograms are generated; the unwrapped phase of the ith pixel on the $m\text{th}(1 \le m \le M)$ differential interferogram can be expressed as [31], [32], [33], [34]

$$\begin{aligned}\Delta\varphi^i &= \Delta\varphi^i_{def} + \Delta\varphi^i_{topo} + \Delta\varphi^i_{atm} \\ &\quad + \Delta\varphi^i_{orbit} + \Delta\varphi^i_{noise} + \Delta\varphi^i_{HP} \\ &\approx \frac{4\pi}{\lambda}\Delta d^i + \frac{4\pi B_i}{\lambda R\sin\theta}\Delta H^i + \Delta\varphi^i_{res} \end{aligned} \tag{1}$$

where $\Delta\varphi^i_{def}$, $\Delta\varphi^i_{topo}$, $\Delta\varphi^i_{atm}$, and $\Delta\varphi^i_{orbit}$ represent the phase component related to deformation, residual topography, atmospheric delay, and orbital error, respectively; $\Delta\varphi^i_{noise}$ refers to the noises; $\Delta\varphi^i_{HP}$ denotes the HP nonlinear deformation component; λ stands for the radar wavelength; and Δd^i is the deformation component along the line of sight of the ith pixel point, which is referred as the low-pass (LP) deformation component. The residual topographic phase is given as $\Delta\varphi^i_{topo} = \frac{4\pi B_i}{\lambda R\sin\theta}\Delta H^i$, where θ and B_i denote the radar incidence angle and the length of the vertical baseline of the ith interferometric pair, respectively; R refers to the distance between the coherent target and the location of the radar satellite; ΔH represents the residual elevation, which is unknown and to be solved for; and $\Delta\varphi^i_{res}$ stands for the final residual phase, which consists mainly of the atmospheric delay phase, the noise phase, and the HP deformation component.

After the time-series interferometric phases in the study area are obtained, the time-series phase signals can be used as the input original signals, and the FastICA algorithm is utilized here to carry out the subsequent decomposition. FastICA is a fast optimization iterative ICA algorithm, which can decompose the time-series phase signals by employing a fixed-point iterative optimization algorithm based on negative entropy maximization [35], [36], [37], [38]. The InSAR time-series phase signal could be expressed as

$$X = A \times S \tag{2}$$

where X represents the mixed signal of the observation, referred as the InSAR times-series phases; A denotes the mixing matrix, each column in which is a eigenvector for each independent component; and S represents the source signals, which is the combination of the independent components. It should be noted that for InSAR data processing, ICA has two different methods in the response domain of InSAR data: sICA and temporal ICA (tICA). sICA focuses on the separation based on the independence of spatial distributions, which considers that multiple regions related to different signals are independent of each other. Comparatively, tICA focuses on the separation based on the independence of the time-series characteristics for the phase signals, which considers that the phase time-series related to

different signals are independent. sICA and tICA have different arrangements of X. For sICA, the mixed signal X composed of images N and pixels C: $X_{N\times C} = A_{N\times n} \times S_{n\times C}$. For tICA, mixed signal of X composed of C lines of pixels and N rows of images: $X_{C\times N} = A_{C\times n} \times S_{n\times N}$. Since the number of time-series InSAR observational data in the spatial dimension is much larger than that of the temporal dimension, and the signals of ground deformations are strongly independent of the noise signals, tICA is computationally more challenging than sICA [15], [16]. Consequently, sICA is more suggested for InSAR signal decomposition.

For sICA, $X = [x_1 x_2 \cdots x_C]$, where the phase on the ith$(0 < i < C)$ image pixel can be expressed as a combination of each independent components: $x_i = (\varphi_i^1, \varphi_i^2, \ldots, \varphi_i^N)^{\mathrm{T}}$. S in (2) can be expressed as follows:

$$S_{n\times C} = [IC_1 IC_2, \ldots IC_n]^{\mathrm{T}} = \begin{pmatrix} \varphi^1_{defo\_fro}, \varphi^1_{defo\_per}, \varphi^1_{atm}, \varphi^1_{orbit}, \ldots, \varphi^1_{noise} \\ \varphi^2_{defo\_fro}, \varphi^2_{defo\_per}, \varphi^2_{atm}, \varphi^2_{orbit}, \ldots, \varphi^2_{noise} \\ \cdots \\ \varphi^C_{defo\_fro}, \varphi^C_{defo\_per}, \varphi^C_{atm}, \varphi^C_{orbit}, \ldots, \varphi^C_{noise} \end{pmatrix}^{\mathrm{T}} \tag{3}$$

where IC_n denotes the nth$(1 < n < N)$ independent component, which includes the permafrost deformation φ_{defo_fro} and φ_{defo_per}, atmospheric delay phase φ_{atm}, orbital error φ_{orbit}, and other related independent components such as noise φ_{noise}.

Substituting (3) to (2), (2) can be written as

$$X_{N\times C} = A_{N\times n} \times S_{n\times C} = A_{N\times n} \times \begin{pmatrix} \varphi_{defo\_fro}{}^1, \varphi^1_{defo\_per}, \varphi^1_{atm}, \varphi^1_{orbit}, \ldots, \varphi^1_{noise} \\ \varphi^2_{defo\_fro}, \varphi^2_{defo\_per}, \varphi^2_{atm}, \varphi^2_{orbit}, \ldots, \varphi^2_{noise} \\ \cdots \\ \varphi^C_{defo\_fro}, \varphi^C_{defo\_per}, \varphi^C_{atm}, \varphi^C_{orbit}, \ldots, \varphi^C_{noise} \end{pmatrix}^{\mathrm{T}} \tag{4}$$

where φ_{defo_fro} and φ_{defo_per} represent the phase associated with the permafrost deformation interested in. For the InSAR phase signals, various types of signals in (4) are statistically independent with each other. Then, an $\mathrm{IC}_i(i = 1, 2, \ldots, n)$ phase matrix $Y_{i,N\times C}$ can be reconstructed by the ith column of the mixing matrix $A_{N\times n}$ (i.e., temporal eigenvector i, TE_i) multiplied by the ith row of the IC_s matrix $S_{n\times N}$. After that, the IC phase matrices $Y_{i,N\times C}(i = 1, 2, \ldots, n)$were related to physical signals such as atmospheric delay error, linear deformation, nonlinear deformation, and periodic deformation. Therefore, the FastICA algorithm can be utilized to separate the independent components from the InSAR times-series phases, and the interested deformation phases can be extracted, which will be used in the following by physical modeling and parameters estimation.

B. Time-Series Modeling and Parameters Estimation

After the separation of the InSAR time-series phase signals, it should determine which model to use based on the characteristics of the signals' temporal eigenvector. They are permafrost long-term linear deformation correlation component φ_{defo_fro} when the separated phase signals are highly linear. In contrast, they are periodic permafrost deformation correlation component φ_{def_per} if the signals are highly seasonal. After that, the deformation-related component in (4) can be expressed as $\varphi_{def} = \varphi_{def\_fro} + \varphi_{def\_per}$, and the multivelocity linear model can be adopted to model the phase associated with linear deformation. The cumulative linear deformation of the ith high coherence point can be written as follows [39]:

$$d_f^i = \sum_{k=1}^{N} v_k \times (t_k - t_{k-1}) \tag{5}$$

where d_f^i represents the permafrost long-term linear deformation at the ith coherence point on the interferogram; v_k is the deformation velocity between neighboring images, treated as unknown parameter; $t_k - t_{k-1}$ stands for the time interval between neighboring images, with $k \in 1, 2, \ldots, N$.

The periodic deformation component caused by the external environment facilitates the application of a deformation model that considers the climatic factors for modeling

$$d_p^i = a_1 \times T(t) + a_2 \times P(t) \tag{6}$$

where d_p^i represents the periodical deformation related to the climatic factors at the ith coherence point on the interferogram; a_1 and a_2 are the unknown coefficients of $T(t)$ and $P(t)$, respectively; and $T(t)$ and $P(t)$ are temperature and precipitation data, respectively. As a result, the total deformation phase φ_{def}^i can be expressed as follows:

$$\varphi_{def}^i = \varphi_{def\_fro}^i + \varphi_{def\_per}^i = \frac{4\pi}{\lambda}(d_f^i + d_p^i) = \frac{4\pi}{\lambda}\left(\sum_{t_A^i+1}^{t_B^i} v_k \times (t_k - t_{k-1}) + a_1 \times T(t) + a_2 \times P(t)\right) \tag{7}$$

where the unknown parameters are $Pa = [v_1, \ldots v_N, a_1, a_2]$, which contains N linear velocities and two environmental parameters. The above equation can be simplified as

$$F = B \times L \tag{8}$$

where F represents the vector of total deformation phases; B is the coefficient matrix: $B = [t_1, \ldots, t_N, T(t), P(t)]$; and L refers to the matrix of all parameters to be solved: $L = [v_1, \ldots, v_N, a_1, a_2]$. The solution of (8) is a least squares (LS) estimation issue. The coefficient matrix B was decomposed by singular value decomposition (SVD) due to its singular problem, to obtain the corresponding full-rank matrix, and then the pseudoinverse of B is solved to compute the least-norm solution for the parameters in L. Based on the solved unknown parameters, the LP deformation, consisting of the linear and periodic components of deformation fitted by a multivelocity linear model and a permafrost deformation model, respectively, can be obtained by submitting them into (7).

C. Flowchart of HPICA Processing Steps

Fig. 1 presents the flowchart of HPICA. First, $N + 1$ SAR images are processed by GAMMA, and the time-series unwrapped

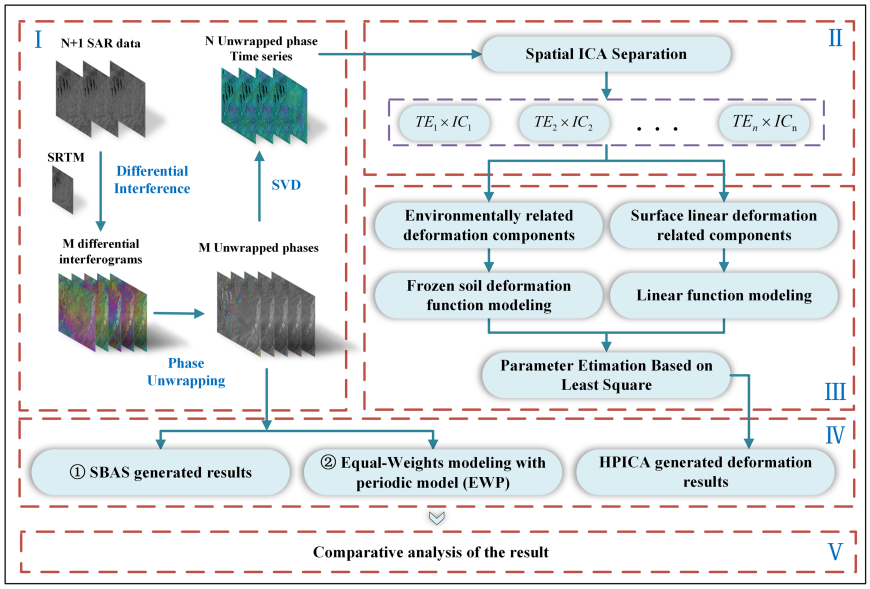

Fig. 1. Flowchart of the HPICA algorithm.

phases can be obtained by differential interferometry. Based on the FastICA method, the independent components (IC_n) and corresponding temporal eigenvectors (TE_n) can be acquired, including the deformation component and the atmospheric and noise components. Second, the deformation components separated in the previous step were modeled by different models, and the multivelocity linear model was applied to the permafrost linear deformation component. While the deformation model that introduced the climatic factors was used for the periodic deformation component. In addition, the unknown parameters were solved by the LS and SVD methods. The time-series deformation results were compared with those obtained by two traditional models based on direct modeling of the total unwrapped phases with different components equal weighted overlap. Finally, the performance of HPICA was compared with those of the conventional methods.

III. Simulated Experiment

To verify the effect of ICA on separating the deformation phases and guiding the real data experiments, a simulated experiment was designed and executed in this article. Five independent components in the original independent signal were assumed. The original signal was simulated based on the components on the right-hand side of (4). The satellite parameters adopted in the experiment were based on Sentinel-1A spaceborne parameters, in which the wavelength was 0.056 m and the time interval was 24 days. Conversely, the linear deformation component was simulated by (5), where the parameter was set using the two-dimensional (2-D) Gaussian simulator with a range of [–40 40] mm/a. In addition, the periodic deformation component was established by (6), where the environmental coefficients a_1 and a_2 were set as 0.01 mm/mm and 0.02 mm/°C, respectively. The orbital error phase was modeled by $z = ax + by + c$, where a, b, and c are normally distributed random numbers. At the same time, the atmospheric delay phase was added in with a range of [–11] rad [40]. Subsequently, the noise phase was modeled using 2-D normal random numbers ranging from −0.5 to 0.5 rad. The five components of the above simulation were blended to generate a study area of 50×50 pixels. Two sedimentation funnels were simulated using the linear and periodic components, and a total of 29 simulated time-series images were acquired over a span of 2 years, with intervals of 24 days. Moreover, both the sICA and tICA were employed to separate the simulated mixed signals.

Fig. 2 illustrates the simulated linear signals, the periodic signals, and some of the separated signals. In the figure, the top three rows ("Original-Linear," "sICA-Linear," and "tICA-Linear") represent the simulated linear signals and the generated linear components obtained after separation by sICA and tICA, respectively, which were treated as real ones. The bottom three rows ("Original-Period," "sICA-Period," and "tICA-Period") display the simulated periodic components and those separated by sICA and tICA, respectively. The linear results after the separation using sICA in the second row are highly similar to the real values in both time and space. Meanwhile, locations of the deformation fields and the deformation trends are consistent with those in the "Original-Linear," showing a more obvious linear trend temporally. The "tICA-Linear" separation in the third row is more different from the simulated linear signal, with an erroneous sedimentation funnel at 24 days. Similarly, the periodic component separated by sICA in the bottom three rows is closer to the original real results. According to our calculation, the root-mean-square errors (RMSE) between the two sets of signal separation results and the original simulated real components indicate that the sICA separation possesses a smaller RMSE than the tICA separation. The mean RMSEs of the linear and periodic components separated by sICA are estimated as ±2.2 and ±1.0 mm, respectively, whereas those of the results separated by tICA are ±5.3 and ±2.7 mm, respectively.

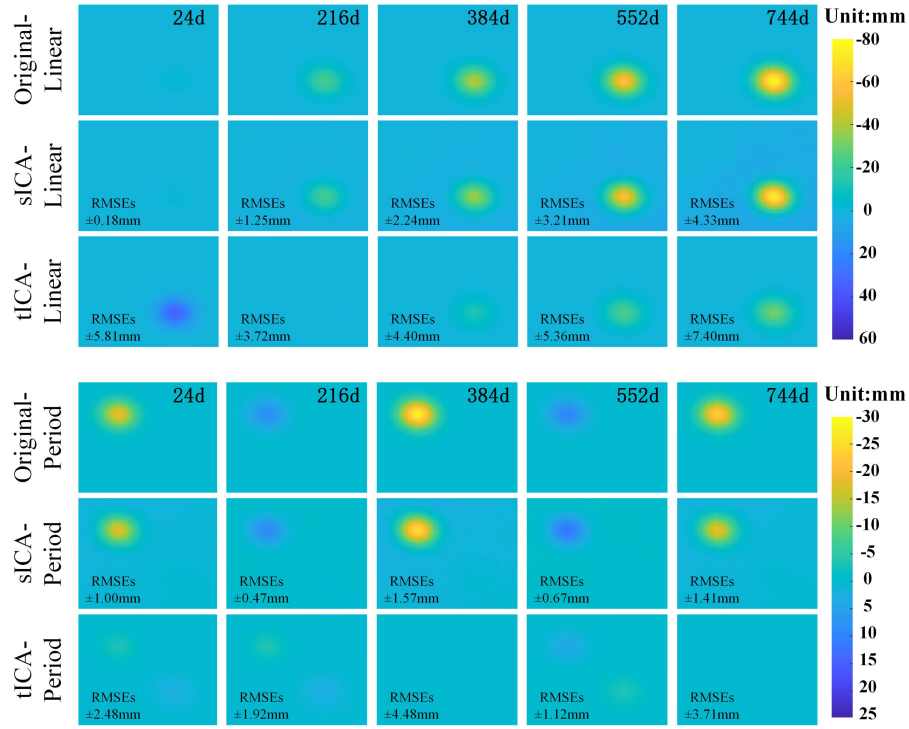

Fig. 2. Comparison of the separated results of sICA and tICA at each temporal date.

Consequently, tICA separation exhibits a significantly higher RMSE in contrast to the sICA separation.

Fig. 3 shows the independent components including the linear (IC_1) and periodic components (IC_2). RMSEs between the deformation signals separated by the sICA and tICA methods and the simulated real deformation signals are compared in the last row of Fig. 3. It explicates that the RMSEs of the sICA separation are smaller than the tICA separation for all the simulated images. Besides, all RMSEs of the sICA method are below 6 mm, with 86% of the images being under 4 mm. In contrast, the tICA method possesses an RMSE of 96.5% within 6–10 mm. Further calculation implies that the mean RMSE of the sICA method is 59.9% lower than that of the tICA method. Experiments have shown that the sICA method can more accurately restore the original signal in comparison to the tICA method, which can be attributed to a higher density in space and relatively sparse density in time of the simulated signals. In addition, it is observed that the spatial independence of the phase components is significantly better than the temporal independence. If signals are correlated in the temporal eigenvectors, the tICA separation will demonstrate a significantly lower accuracy compared with the sICA. Consequently, the sICA separation method was chosen in the subsequent real experiments.

IV. Real Data Experiment

A. Study Area and Data Processing

The Qinghai–Tibetan Plateau is the largest area of permafrost in the world in low- and mid-latitudes. Compared with the permafrost in the polar regions, the permafrost in this area is particularly sensitive to the climate and is highly susceptible to the influence of the environment due to thinner thickness and higher temperature [1], [41], [42]. Located on the Qinghai–Tibetan Plateau, the Gongyu Highway is an important part of the "One longitudinal, one transversal, and two interconnecting" highway network of the Yushu Earthquake Recovery and Reconstruction Master Plan. Its starting point is located in the town of Qiapu, Republican County of Hainan Tibetan Autonomous Prefecture in Qinghai, and the end point is located in the town of Jiegu, Yushu County of Yushu Tibetan Autonomous Prefecture in Qinghai. The total length of permafrost of Gongyu Highway is 227 km, accounting for more than one-third of the total length of 634.8 km [43], [56].

The study area is the Maduo section of the Gongyu Highway in Qinghai. Fig. 4 shows the specific location of the study area and on the SAR satellite images. In Fig. 4(a), the range of Sentinel-1A ascending data covering the survey area is marked in a red rectangle, and the purple rectangle indicates the cropping range of this experiment. Fig. 4(b) displays the concrete location of the cropped area in Qinghai Province. Fig. 4(c) shows the location of the cropped area on the Google Map. Related studies have demonstrated that there is a large amount of seasonally frozen ground and permafrost in this area, accounting for about 50% of the permafrost. With complex and diverse soil types on the surface, and the study area is dominated by wide valleys, river, and lake basins formed by fault subsidence. The altitude of this area is about 4200–4300 m, and there are many lakes, and the Yellow River flows through this area, so it is rich in water resources [44]. Under the background of the greenhouse effect,

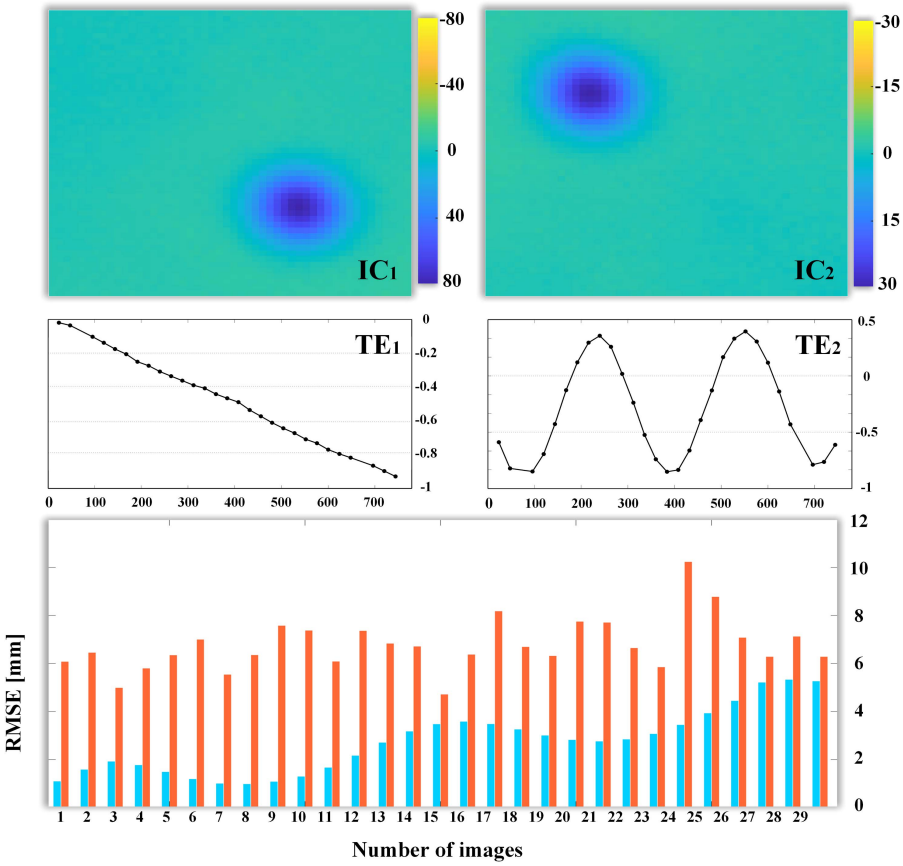

Fig. 3. Simulation test for ICA separated results (top left: linear independent component (IC_1); top right: periodic independent component (IC_2); middle left: temporal eigenvectors of linear component (TE_1); middle right: temporal eigenvectors periodic component (TE_2). An independent component deformation can be calculated by multiplying numerical values of independent component (top) and its corresponding temporal eigenvectors (middle); bottom: comparison of RMSE of deformation results from sICA and tICA methods separation on simulated 29 images).

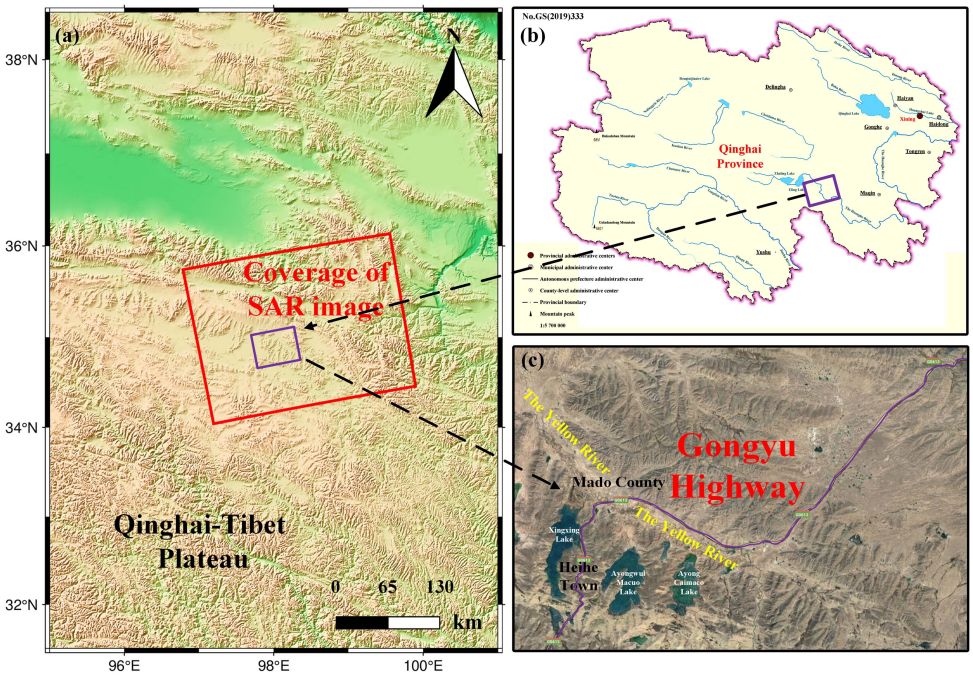

Fig. 4. Study area (purple rectangular) and SAR spatial coverage (red rectangular).

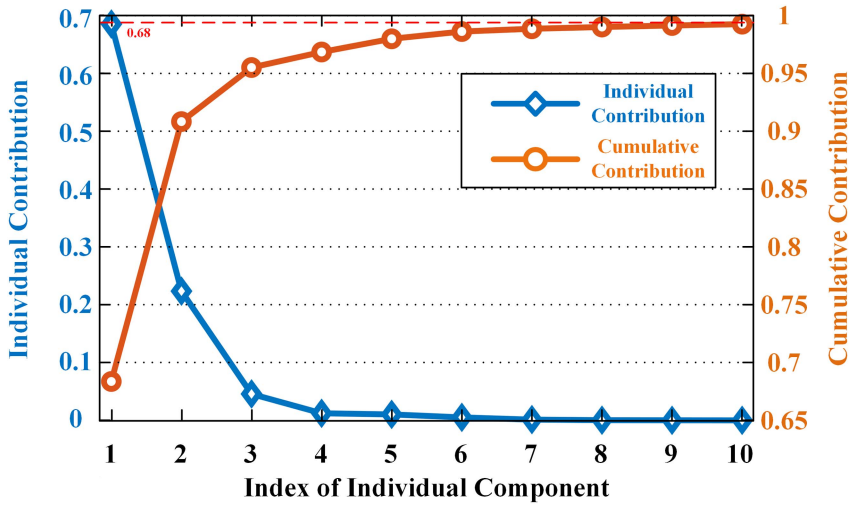

Fig. 5. Contribution of each independent component and the cumulative contribution.

the surface permafrost was degraded by heat and thus collapsed, forming a depression. As a result, the permafrost melts and water accumulates, generating thermokarst lakes. Thermal energy from these thermokarst lakes further affects the surrounding ecosystem by releasing more greenhouse gases from the melting of permafrost and subsurface ice, thus expanding and deepening these lakes [45], [46], [47], [48]. The harsh natural environment and sparse population in this region hinder the implementation of conventional ground-based monitoring with regular access to the ground. Therefore, it is of great importance to implement large-scale deformation monitoring in this region using time-series InSAR technology.

In all, 52 Sentinel-1A (ascending) images were obtained from January 2020 to January 2022. The differential interferometric analysis was conducted using the Swiss GAMMA software. In the experimental processing, the temporal baseline threshold and spatial baseline threshold were set as 150 days and 300 m, respectively, and the multilook ratio was 5:1. The Shuttle Radar Topography Mission Digital Elevation Model with a resolution of 30 m was selected to remove the topographic phase. The polynomial fitting method was adopted to remove the track error and the Gaussian filter was served to filter the phase to suppress the noise. In addition, the minimum cost flow method was used for phase unwrapping.

B. InSAR Phase ICA

Before the phase ICA, the number of ICA separated components in the real experiment should be determined first. The contributions of each independent component and the cumulative contribution were calculated as shown in Fig 5. In Fig. 5, the *X*-axis indicates the calculated contribution of 10 components, and the left and right *Y*-axes are the scale of individual component contribution and cumulative contribution, respectively. The points on the solid red line with diamonds indicate the contribution of each component, and those on the solid blue line with circles are the cumulative contributions. According to our quantitative calculation, the contribution rates of the first five components are 68.4%, 22.4%, 4.66%, 1.34%, and 1.14%, respectively, showing a cumulative contribution of 97.8%. In contrast, the cumulative contribution of the rest of the components is only 2.2%. This indicates that when the number of separated components n in (4) is set to 5, these five components can basically characterize the total phase signal. Therefore, the number of separated components is set to 5 in the subsequent experiments.

Fig. 6 illustrates the results of separated InSAR phase signals by FastICA decomposition. The top figures represent the independent components of the separated components and the bottom ones represent the temporal responses. The temporal eigenvectors were all normalized from -1 to 1. As it shows, IC_1 shows a significant temporal linear variation pattern in the temporal eigenvectors, thus it is presumed to be related to the long-term linear deformation caused by the internal factors. Comparatively, both IC_2 and IC_3 show more spatial correlation characteristics with the topography, and irregularly fluctuations for the temporal eigenvector values around 0, which means that IC_2 and IC_3 have no common temporal responses (positive or negative) in time-series InSAR measurements. Consequently, those two IC components were suggested related to tropospheric delay effects and partly some residual orbital errors [22], [50]. As for IC_4, the independent component exhibits similar spatial distribution characteristics as that of IC_1, and most of the temporal eigenvector values are positive with a nonlinear variation. Thus, IC_4 was hypothesized as the nonlinear deformation signals remained in the residual phase components. Comparatively, IC_5 shows a significant apparent trend of periodic variation, which was assumed related to the deformation component associated with external climatic factors.

To verify the speculation of IC_2 and IC_3 based on the above analysis, the sum of the two components was compared with the GACOS atmospheric data. In the experimental processing, first, the GACOS data were interpolated by a 2-D interpolation method to keep a consistent resolution with the Sentinel-1A

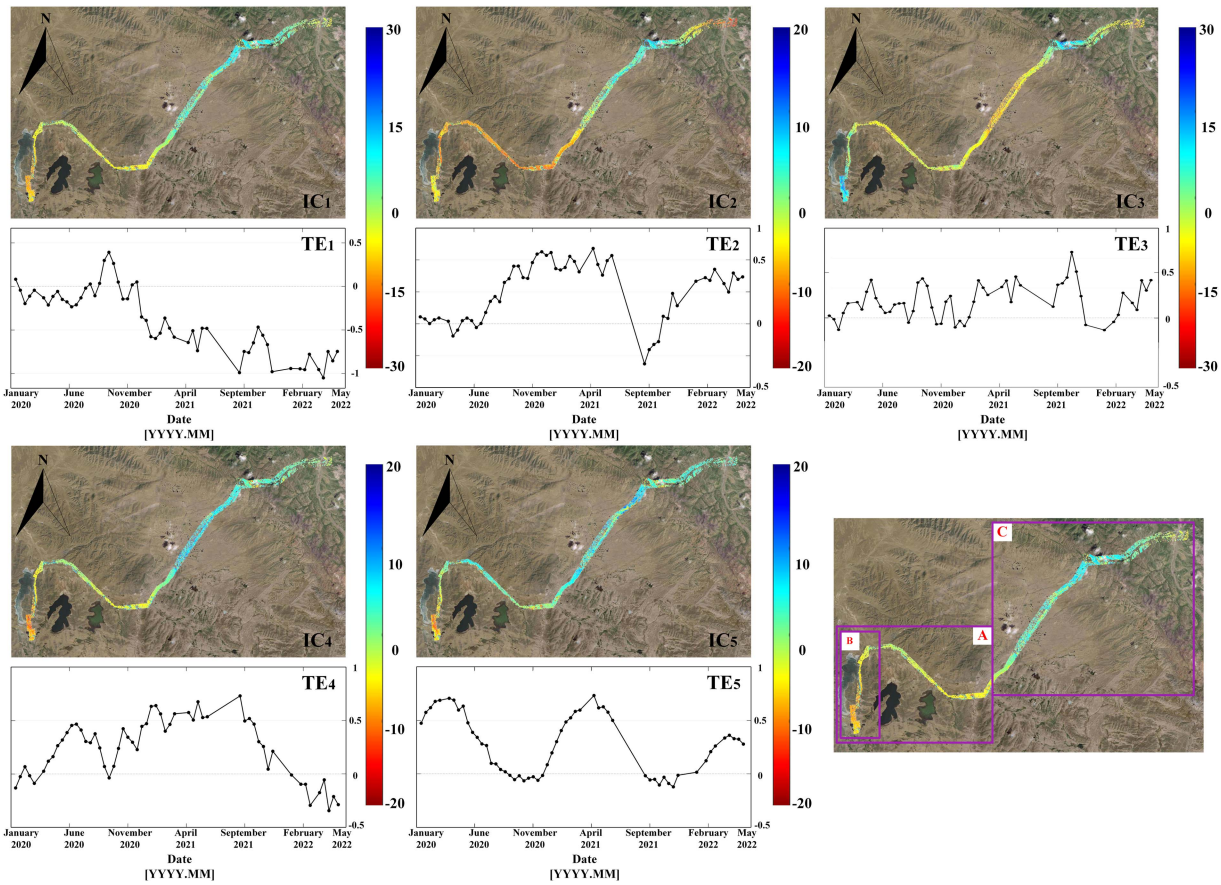

Fig. 6. Independent components $\mathrm{IC}_1 - \mathrm{IC}_5$ and its corresponding temporal eigenvector. An $\mathrm{IC}_i (i = 1, 2, \ldots, n)$ phase matrix $Y_{i,N\times C}$ composed of N images and C pixels can be reconstructed by the ith column of the mixing matrix $A_{N\times n}$ multiplied by the ith row of the IC_s matrix $S_{n\times N}$. The IC phase matrices $Y_{i,N\times C} (i = 1, 2, \ldots, n)$ can be related to physical signals such as linear deformation (IC_1), atmospheric delay error ($\mathrm{IC}_2 + \mathrm{IC}_3$), nonlinear deformation (IC_4), periodic deformation (IC_5) based on the spatiotemporal characteristics of the IC_s and temporal eigenvectors.

data. Then, both the GACOS data and the two independent components were spatially normalized to a stable reference point on the first temporal image. Finally, the average atmospheric phases at the points distributed over the study area were masked out and calculated manually, in order to keep the identical spatial ranges of the two datasets.

The comparative results are shown in Fig. 7, where Fig. 7(a) shows the calculated average deformations generated by $\mathrm{IC}_2 + \mathrm{IC}_3$ components, and Fig. 7(b) by the GACOS atmospheric data. As it shows, GACOS atmospheric data and the deformation generated by $\mathrm{IC}_2 + \mathrm{IC}_3$ are highly consistent in spatial distribution: both characterized by obvious subsidence (dark red color) in region B with a maximum value of about –50 mm; both dominated with blue color in region C where locates the mountainous areas in the northeast of the Gongyu Highway, with slow subsidence of about –20 mm and an uplift of 20 mm in the southwest of region C. Conversely, the two figures still show differences in the area close to the Yellow River. It may be caused by the phase unwrapping inaccuracy and residual orbital errors in the study area. Therefore, the comparisons prove our hypothesis that the $\mathrm{IC}_2 + \mathrm{IC}_3$ components are topography-related atmospheric delay effects, partly some residual orbital errors, and the phase unwrapping error in region A.

To verify the correlation between IC_5 and climatic factors in the region, the correlation coefficients between IC_5 and temperature and precipitation were calculated, as demonstrated in Fig. 8. The precipitation data, temperature data, and IC_5 component are marked with a blue bar, orange solid line, and black solid line with triangles, respectively. Fig. 8 discloses that IC_5 has a high correlation with both temperature and precipitation simultaneously. The correlation coefficients of IC_5 with temperature and precipitation were calculated to be 0.532 and 0.358, respectively. Meanwhile, a two-month lagging effect between IC_5 and the climatic factors can be found on the graph. Further, two correlation coefficients can be improved to 0.795 and 0.819, respectively, after the correction for the lag. This confirms the hypothesis that IC_5 is an environmentally relevant deformation component.

C. Analysis of the Generated Total Time-Series Deformation via HPICA

Fig. 9 outlines the parameters of the study area obtained by the method flow described in Section II-B. Fig. 9(a) represents the average value of the linear rates in the multivelocity model at each high-coherence point, and Fig. 9(b) and (c) represents

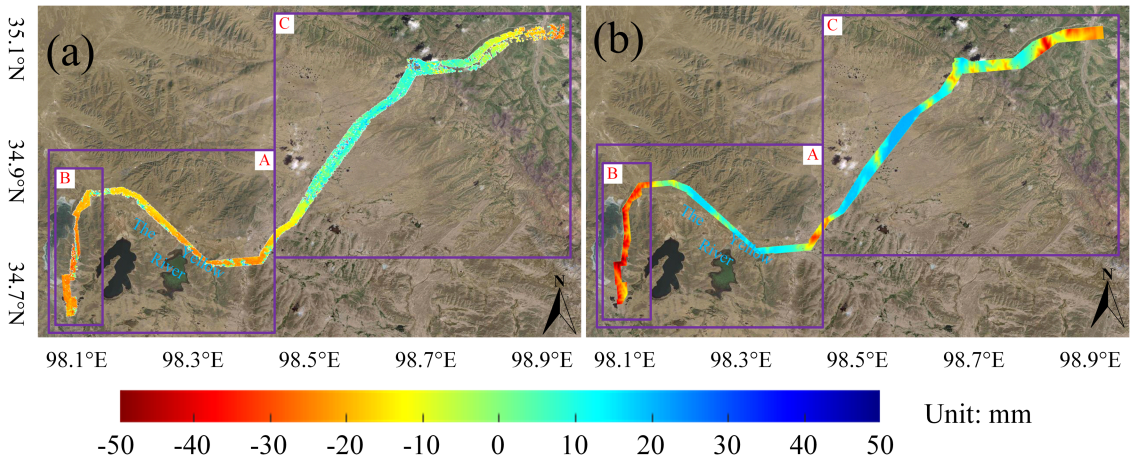

Fig. 7. Comparison of deformations generated by the sum of IC_2 and IC_3 with GACOS atmospheric data [(a) Deformations generated by $IC_2 + IC_3$. (b) Average deformations generated by GACOS atmospheric data].

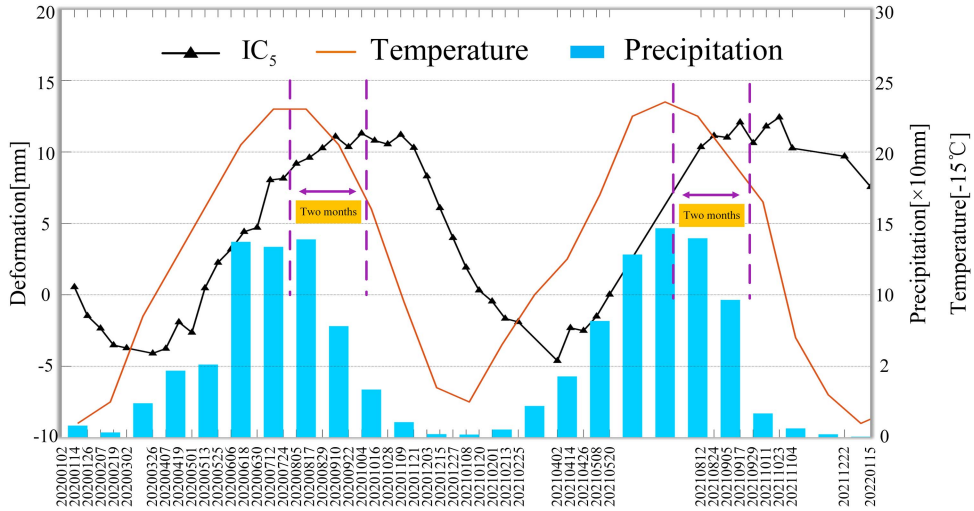

Fig. 8. Correlation analysis of IC_5 with climatic factors.

the estimation of the temperature and precipitation parameter in the model of permafrost deformation considering the climatic factors at the high-coherence point, respectively. Fig. 9(d) shows the HPICA generated deformation in A. Fig. 9 displays that the deformation in B is very pronounced. In Fig. 9(a), the average rate is distributed in the range of [–40 40] mm/a, and that is larger in the B near the lake, as shown by the color bar, corresponding to the value of the interval of [–30 –20] mm/a. The average rate is smaller in the area farther away from the lake, which corresponds to a value of about –10 mm/a according to the yellow color. Fig. 9(b) and (c) indicates that the effects of the temperature and precipitation parameters are more concentrated in the southwestern part of B. The ranges of the two parameters are [–0.30.2] mm/°C and [–0.08 0.06] mm/mm, correspondingly. The color in the area away from the lake is mostly green, where values of the two parameters fluctuate around zero. Fig. 9(b) and (c) suggests that the temperature parameter has a larger value than the precipitation, which indicates that the temperature has a greater effect on the generation of deformation compared with the precipitation. Such findings are consistent with the fact that permafrost is very sensitive to temperature.

Fig. 10 shows the time-series deformation from January 2020 to April 2022 for the study area. From the spatial distribution of colors, the deformation of the whole region is dominated by subsidence, in which a large amount of deformation is mainly reflected in area B near the Star Lake, and the maximum subsidence in the whole time is –149.9 mm. The deformation of the rest area is mainly around [–20 20] mm. The generation of large-scale deformation in B is mainly caused by the long-term displacement of internal factors and the multiple effects of external climatic factors. Thanks to the Sea of Stars, the surface of the region is “warm” all year round. The low topography of the region and the abundant recharge from groundwater and river, as well as the significantly higher water and ice content of the permafrost layer, the region becomes more susceptible to climatic factors (especially temperature) and responds more

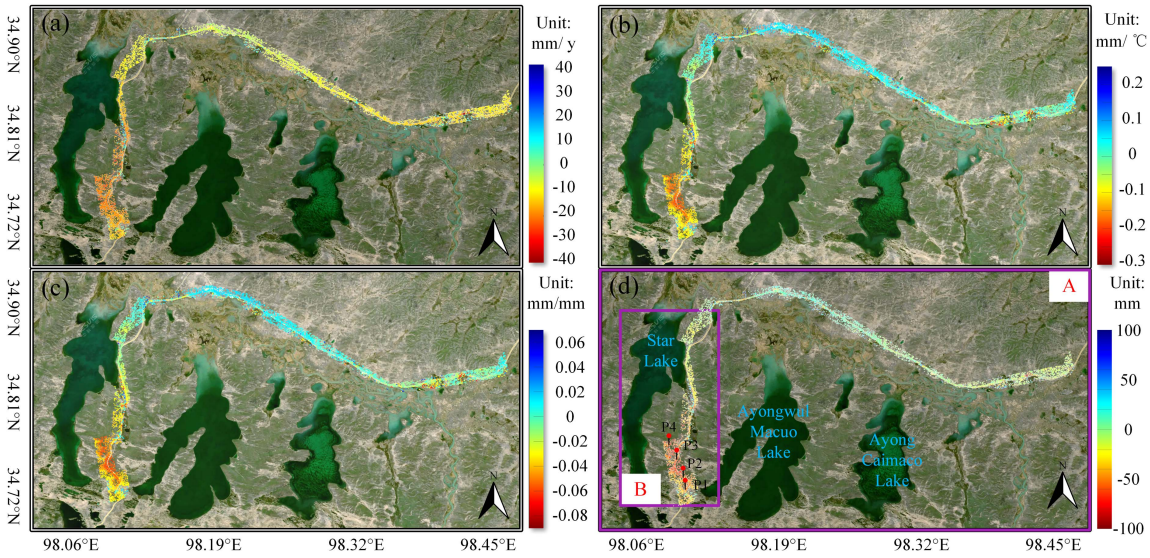

Fig. 9. Estimated parameters [(a) Average rate v. (b) Temperature parameters a_1. (c) Precipitation parameters a_2. (d) Deformation results: 20200102–20220115].

intensely. The maximum deformation in B from April 2020 to September 2020 could be visualized from the color change on the time-series figure, whereas the deformation in the rest of the area was small or insignificant. The deformation region experienced an obvious raise during the cold season from late 2020 to early 2021. During the high summer temperatures in May–November 2021, there is significant subsidence in area B. In the cooler periodic from November 2021 to early 2022, there exists subsidence slows down and some amount of raise. The deformation in this region is clearly periodic with the seasons, which is very consistent with the deformation mechanism of permafrost.

D. Accuracy Analysis

Since there is no external level data in this area, the annual average subsidence velocity calculated in the previous study is –6.9 mm/a, which is in good agreement with the results of subsidence monitoring in Maduo area of Qinghai [44]. The size of residual phases can reflect the modeling accuracy between the InSAR modeling results and the real deformation: the smaller residuals in the interferometric pairs are, the higher the modeling accuracy is [8], [34]. The initial residual phases are obtained by subtracting the original total interferometric phases from the modeled LP deformation phases. After that, the residual phases are spatio–temporal filtered to obtain the HP nonlinear deformation component. The remaining components are the final residual phases of each interferometric pair. The residual phases of the HPICA were compared with those of the SBAS-InSAR and the Equal-Weights modeling with Periodic model (EWP) without ICA separation. As illustrated in Fig. 11, the HPICA method exhibits the residual phases of all less than 0.6 rad and 94.2% of it are less than 0.3 rad. In contrast, the residual phases of the SBAS results are all less than 1 rad, and 63.5% of it are less than 0.3 rad. Therefore, the comparison here indicates that residual phases of the periodic model are all less than 1.6 rad, and only 7.7% of it are less than 0.3 rad. The modeling accuracy of HPICA is 60% and 84.7% higher than the SBAS and the periodic model, respectively. The results reveal that the deformation components can be separated more accurately after filtering out the atmospheric delay and orbital error residuals by ICA separation, and the accuracy of the final deformation estimation can also be significantly improved due to the more precise related phase components.

V. Discussions

A. Potential Reasons for the Derived Deformation

The potential reasons for the derived deformation can be divided into external factors and internal factors. The external factors include temperature, precipitation, and humidity solar radiation. Temperature and precipitation are the main factors affecting the properties and distribution of permafrost in high mountainous areas. The periodic change of temperature is an important causative factor for the periodic deformation of permafrost. The internal factors mainly include geotectonic activities, with the break zones in the Qinghai–Tibetan Plateau still in the process of activity and susceptible to complex influences on the active geology of the region.

In this article, the main deformation area is located in the northeastern part of the Tibetan Plateau, with an altitude of about 4200–4800 m. The Xingxiuhai Sea, Star Lake, and the Yellow River provide abundant water resources for the permafrost in the region [44]. The reason for seasonal fluctuation is mainly the increase in summer temperature and precipitation. Heat absorption and melting of the active layer lead to an increase in its water content. Meanwhile, the heat and water are transported from the top to the bottom simultaneously, thinning the entire active layer and resulting in consequent subsidence of the ground surface. Consequently, a significant subsidence was discovered in B from April 2020 to September 2020, and from May 2021 to November 2021. In winter, the unfrozen water and heat

Fig. 10. Time-series deformation results over the study area.

in the active layer migrate upward when the temperature and precipitation decrease. As unfrozen water begins to freeze in the upper part of the active layer because of the extremely low surface temperatures, therefore, the active layer becomes thicker and subsidence is slowed and raised. Accordingly, the subsidence in B slows down and rises during the cold periodic from late 2020 to early 2021 and from November 2021 to early 2022.

To further analyze the time-series characteristics of the deformation in B, four characteristic points [P1–P4 marked in Fig. 9(d)] were selected for the quantitative analysis. Subsequently, the results were compared with the temperature and precipitation, as illustrated in Fig. 12. The four feature points show the same subsidence movement over the whole periodic. Furthermore, it displays a large temporal correlation and is accompanied by a very obvious periodic feature. The whole study period can be divided into two periods of one year. Warm season: From May 2020 to October 2020 and May 2021 to October 2021, all four points appeared obvious subsidence at high temperatures and fast precipitation velocity. The subsidence velocity at P3 was the fastest, reaching –168.8 mm/a from 8 May 2021 to 11 October 2021, with a cumulative maximum subsidence of –72.2 mm. Cold season: The content of unfrozen water in the active permafrost layer was reduced under the low temperature and precipitation from October 2020 to May 2021 and from October 2021 to mid-March 2022, as a result, all the features were raised, with the largest raise of 28 mm from October 4, 2020 to May 8, 2021 at P1.

B. *Frozen Soil Type Identification Based on sICA*

As introduced in the paper [50], [51], according to the length of time the frozen state of the soil is being maintained, permafrost can generally be categorized into short-term permafrost,

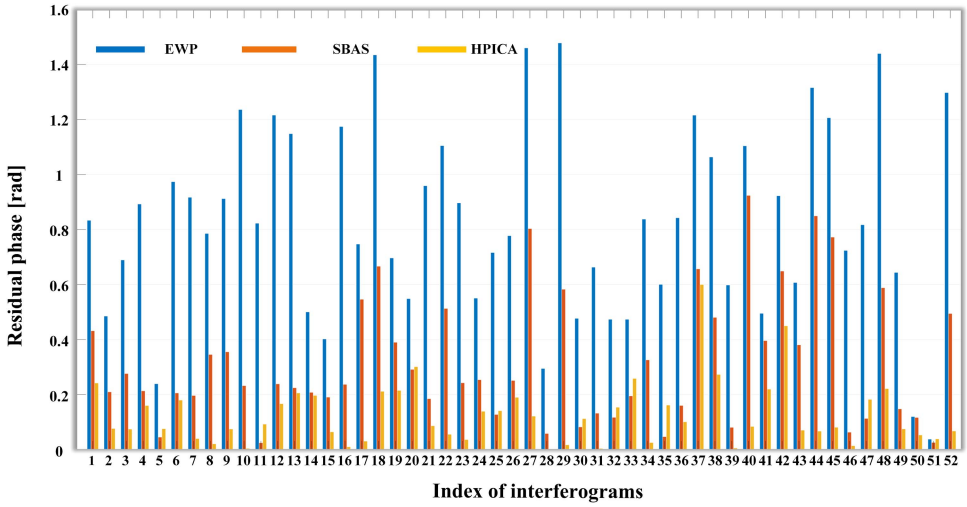

Fig. 11. Residual phase comparison of 52 SAR images between the HPICA method and two commonly used traditional methods.

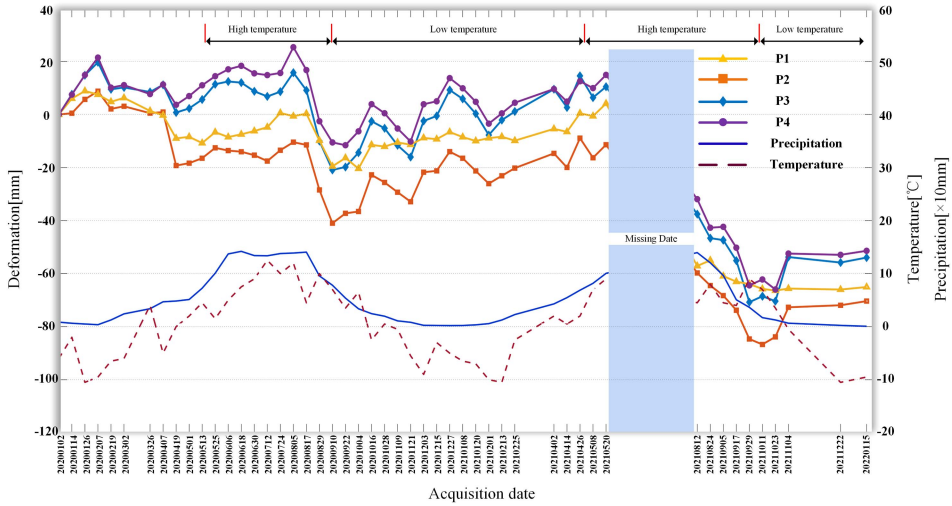

Fig. 12. Time-series settlement on feature points based on HPICA.

seasonal permafrost, and permanent permafrost. The permafrost remains frozen for several years or even tens of thousands of years, which temperature of the soil layer always stays below 0°C and the permafrost layer does not melt all year round. As a result, the permafrost is relatively stable. Seasonal permafrost refers to permafrost that remains frozen for half a month or several months, which time of existence is shorter than permanent permafrost. Seasonal permafrost is so unstable that it is more susceptible to the effects of temperature and precipitation [52], [53], [54], [55]. According to the spatial distribution characteristics of $IC_1 + IC_5$ in Fig. 13(b) in this study, it can be found that area A is a significant deformation region. The seasonal deformation in A is 55.7% higher than that in region C by calculation. The maximum seasonal deformation in A reaches –40 mm, which is significantly higher than C. This suggests that the influence of seasonal deformation is much higher in A than in C, which is consistent with the instability of seasonal permafrost and the obvious seasonal deformation above. Therefore, it is inferred that the seasonal permafrost is mainly distributed in A. In contrast, the seasonal and total deformation in C is smaller than A, so it is assumed that the soil distributed in C is permanent permafrost dominantly.

To verify the accuracy of the above conclusions, IC_1 and IC_5 were compared with the existing permafrost classification results introduced in [49]. Fig. 13(a) shows the distribution map of permafrost on the Tibetan Plateau studied by previous researchers. The extent of the study area of Maduo was cropped according to the latitude and longitude in ArcGIS software, in which the dark blue color denotes the permanent permafrost and the orange color denotes the seasonal permafrost. Fig. 13(b) shows the sum of the linear component and the periodic component in Fig. 6. Areas A and C in the figure suggest that there is a large amount of seasonal permafrost in area A in the southwestern part of the Maduo region, whereas permanent permafrost distributes in the

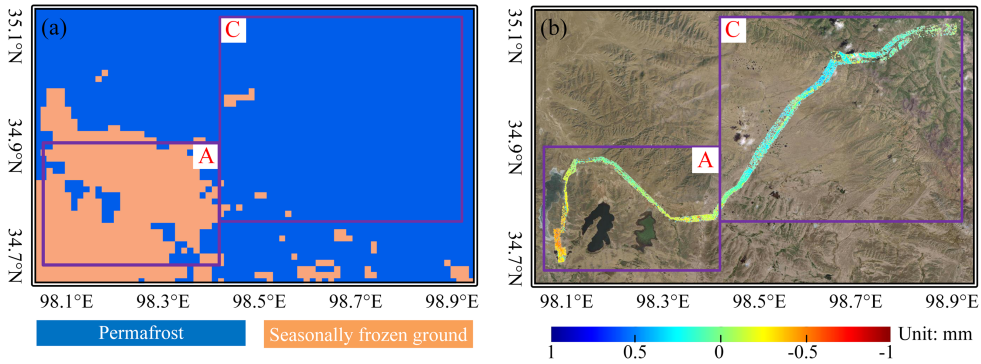

Fig. 13. Frozen soil type distribution map comparison [(a) Map of the thermal stability of permafrost on the Tibetan Plateau [51]. (b) Sum of IC_1 and IC_5].

northeastern part. This observation shows consistency with the boundary of the two types of permafrost zones that are separated by the results of this article in Fig. 13(b).

C. Applicability Analysis for HPICA

1) The FastICA method can accurately separate the independent components in the InSAR phase, which is conductive to removing atmospheric delays, topographic residuals, and orbital errors from the unwrapped phase. Thereby, the deformation-related phase interested in can be more accurately extracted. Meanwhile, it can assist in determining the weights of deformation-related signals with different physical causes, thus decreasing modeling errors caused by assumptions in equal weights for direct modeling.
2) The simulation experiments in Section III demonstrate that the sICA is significantly better than the tICA in separating the InSAR signals. This can be attributed to the high spatial density of high coherence points on the interferograms of each view and the high spatial resolution and visible boundary information. Conversely, the time-series is limited by the revisit period of the SAR satellite and the sampling density is low. This permits the sICA to more effectively reveal the information on time-series expansion trends and spatial variations in the spatial distribution of high-coherence points. However, the tICA method can separate better under the context of high-density time-series data (i.e., GNSS data) [56].
3) HPICA can reveal the boundaries of different permafrost regions according to the nature of permafrost, thus facilitating the spatial classification of different types of soil regions. Further, it can assist in modeling the physical deformation of different types of soils, extracting the time-series deformation of permafrost with consideration of the spatio–temporal heterogeneity, and improving the accuracy of deformation estimation.

VI. Conclusion

An improved method for estimating road deformation in permafrost regions was proposed in this article, namely, HPICA. This article utilized FastICA to separate the original unwrapped phase of InSAR, then extracted the relevant components of permafrost deformation by signal feature discrimination and performed physical modeling. Meanwhile, the multivelocity linear model was employed to model the deformation caused by internal factors of permafrost, and a model considering the climatic factors was used to model the relevant environmental components. The LS and SVD methods were employed to estimate the deformation parameters and obtain the final time-series of the deformation.

The simulation experiments explicate that sICA can extract the deformation-related phase components more precisely than tICA method, and the original signal can be better reproduced. The real experiment was carried out based on 52 Sentinel-1A images covering the Maduo section of the Gongyu Highway on the Tibetan Plateau. The total deformation time-series of the study area from January 2020 to January 2022 was obtained. The maximum cumulative deformation is –140.8 mm, and the average annual deformation velocity is –6.9 mm/a, which is 62.5% and 85.7% higher than that of SBAS-InSAR and the EWP without ICA separation, respectively. In addition, the HPICA method can effectively distinguish the boundary between the permanent permafrost and seasonal permafrost regions in Maduo section of Gongyu Highway, demonstrating similar results with the existing results. The method applied in this article can effectively extract the deformation-related components and improve the accuracy of deformation estimation in permafrost compared with the traditional method of direct physical modeling for unwrapped phase, which is conducive to the deformation interpretation for permafrost areas. HPICA can also provide support for highway construction and management and disaster evaluation in the plateau permafrost region.

Acknowledgment

The authors would like to thank the European Space Agency for providing the Sentinel-1A satellite images.

References

[1] Y. H. Ran et al., "Mapping the permafrost stability on the Tibetan Plateau for 2005–2015," *Sci. China Earth Sci.*, vol. 64, no. 1, pp. 62–79, Nov. 2020.
[2] X. Y. Zhou, C. Y. Zhao, N. Li, M. Y. Liu, Y. Cui, and X. Ao, "Influence of snow and temperature on the depth of frozen soil in winter half year in Northeast China," *J. Glaciol. Geocryol.*, vol. 43, no. 4, pp. 1027–1039, 2021.

[3] D. L. Luo, Q. B. Wu, H. J. Jin, S. S. Marchenko, L. Z. Lü, and S. R. Gao, "Recent changes in the active layer thickness across the northern hemisphere," *Environ. Earth Sci.*, vol. 75, no. 7, pp. 1–15, Mar. 2016.
[4] Z. Sun et al., "Influence of lower boundary conditions on the numerical simulation of permafrost temperature field changes," *J. Glaciol. Geocryol.*, vol. 43, no. 2, pp. 357–369, 2021.
[5] Z. Y. Hong and S. G. Jin, "Permafrost deformation in Qinghai-Tibet Plateau time-series PS-InSAR," *Bull. Surveying Mapping*, no. 1, pp. 35–40, 2021.
[6] S. C. Jia, Y. J. Zhang, C. Y. Fan, L. Liu, and W. W. Shao, "Research progress of InSAR technology in permafrost," *Adv. Earth Sci.*, vol. 36, no. 7, pp. 694–697, Jul. 2021.
[7] X. F. Zhang et al., "Time-series InSAR monitoring of permafrost freeze-thaw seasonal displacement over Qinghai–Tibetan Plateau using Sentinel-1 data," *Remote Sens.*, vol. 11, no. 9, Apr. 2019, Art. no. 1000.
[8] R. Zhao, Z. W. Li, G. C. Feng, Q. J. Wang, and J. Hu, "Monitoring surface deformation over permafrost with an improved SBAS-InSAR algorithm: With emphasis on climatic factors modeling," *Remote Sens. Environ.*, vol. 184, pp. 276–287, Oct. 2016.
[9] S. Wang, B. Xu, W. Shan, J. Shi, Z. Li, and G. Feng, "Monitoring the degradation of island permafrost using time-series InSAR technique: A case study of Heihe, China," *Sensors*, vol. 19, no. 6, Mar. 2019, Art. no. 1364.
[10] Y. X. Chen, L. M. Jiang, L. L. Liang, and Z. W. Zhou, "Monitoring permafrost deformation in the upstream Heihe River, Qilian mountain by using multi-temporal Sentinel-1 InSAR dataset," *Chin. J. Geophys.*, vol. 62, no. 7, pp. 2441–2454, 2021.
[11] S. S. Li, Z. W. Li, J. Hu, Q. Sun, and X. Y. Yu, "Investigation of the seasonal oscillation of the permafrost over Qinghai-Tibet plateau with SBAS-InSAR algorithm," *Chin. J. Geophys.*, vol. 56, no. 5, pp. 1476–1486, 2013.
[12] Y. H. Zhang, H. Wu, and G. Sun, "Deformation model of time series interferometric SAR techniques," *Acta Geodaetica et Cartographica Sin.*, vol. 41, no. 6, pp. 864–869, Dec. 2012.
[13] X. M. Xing et al., "Predicting mining-induced dynamic deformations for drilling solution rock salt mine based on probability integral method and Weibull temporal function," *Int. J. Remote Sens.*, vol. 42, no. 2, pp. 639–671, Nov. 2020.
[14] Z. Yang et al., "An InSAR-based temporal probability integral method and its application for predicting mining-induced dynamic deformations and assessing progressive damage to surface buildings," *IEEE J. Sel. Topics Appl. Earth Observ. Remote Sens.*, vol. 11, no. 2, pp. 472–484, Feb. 2018.
[15] S. K. Ebmeier, "Application of independent component analysis to multi-temporal InSAR data with volcanic case studies," *J. Geophys. Res. Solid Earth*, vol. 121, no. 12, pp. 8970–8986, Dec. 2016.
[16] X. M. Xing, L. J. Zhu, B. Liu, W. Peng, R. Zhang, and X. J. Ma, "Measuring land surface deformation over soft clay area based on an FIPR SAR interferometry algorithm—A case study of Beijing Capital International Airport (China)," *Remote Sens.*, vol. 14, no. 17, Aug. 2022, Art. no. 4253.
[17] A. Hyvarinen, "Independent component analysis: Recent advances," *Philos. Trans. Roy. Soc. A, Math., Phys., Eng. Sci.*, vol. 371, no. 1984, Feb. 2013, Art. no. 20110534.
[18] P. Comon, "Independent component analysis, A new concept?," *Signal Process.*, vol. 36, no. 6, pp. 287–314, Apr. 1994.
[19] C. Jutten and J. Herault, "Blind separation of sources, Part I: An adaptive algorithm based on neuromimetic architecture," *Signal Process.*, vol. 24, no. 1, pp. 1–10, 1991.
[20] P. Comon, C. Jutten, and J. Herault, "Blind separation of sources, Part II: Problems statement," *Signal Process.*, vol. 24, no. 1, pp. 11–20, Jul. 1991.
[21] J. Chen et al., "Increased water content in the active layer revealed by regional-scale InSAR and independent component analysis on the central Qinghai-Tibet Plateau," *Geophys. Res. Lett.*, vol. 49, no. 15, Aug. 2022, Art. no. e97586.
[22] M. E. Gaddes, A. Hooper, M. Bagnardi, H. Inman, and F. Albino, "Blind signal separation methods for InSAR: The potential to automatically detect and monitor signals of volcanic deformation," *J. Geophys. Res. Solid Earth*, vol. 123, no. 11, pp. 10226–10251, Nov. 2018.
[23] K. Zhu, X. Zhang, Q. Sun, H. Wang, and J. Hu, "Characterizing spatiotemporal patterns of land deformation in the Santa Ana Basin, Los Angeles, from InSAR time-series and independent component analysis," *Remote Sens.*, vol. 14, no. 11, May 2022, Art. no. 2624.
[24] M. M. Peng et al., "Mapping land subsidence and aquifer system properties of the Willcox Basin, Arizona, from InSAR observations and independent component analysis," *Remote Sens. Environ.*, vol. 271, 2022, Art. no. 112894.
[25] L. Liu, T. J. Zhang, and J. Wahr, "InSAR measurements of surface deformation over permafrost on the North Slope of Alaska," *J. Geophys. Res., Earth Surf.*, vol. 115, no. F3, Sep. 2010, Art. no. F03023.
[26] L. Liu, K. Schaefer, T. Zhang, and J. Wahr, "Estimating 1992–2000 average active layer thickness on the Alaskan North Slope from remotely sensed surface subsidence," *J. Geophys. Res.*, vol. 117, no. F1, Jan. 2012, Art. no. F01005.
[27] S. Daout, M. Doin, G. Peltzer, A. Socquet, and C. Lasserre, "Large-scale InSAR monitoring of permafrost freeze-thaw cycles on the Tibetan Plateau," *Geophys. Res. Lett.*, vol. 44, no. 2, pp. 901–909, Jan. 2017.
[28] J. Chen, L. Liu, T. J. Zhang, B. Cao, and H. Lin, "Using persistent scatterer interferometry to map and quantify permafrost thaw subsidence: A case study of Eboling Mountain on the Qinghai-Tibet Plateau," *J. Geophys. Res.*, vol. 123, no. 10, pp. 2663–2676, Oct. 2018.
[29] Y. F. Hu, L. Liu, K. M. Larson, K. M. Schaefer, J. H. Zhang, and Y. B. Yao, "GPS interferometric reflectometry reveals periodic elevation changes in thaw and freezing seasons in a permafrost area (Barrow, Alaska)," *Geophys. Res. Lett.*, vol. 45, no. 11, pp. 5581–5589, Jun. 2018.
[30] Z. W. Li et al., "InSAR analysis of surface deformation over permafrost to estimate active layer thickness based on one-dimensional heat transfer model of soils," *Sci. Rep.*, vol. 5, Oct. 2015, Art. no. 15542.
[31] P. Berardino, G. Fornaro, R. Lanari, and E. Sansosti, "A new algorithm for surface deformation monitoring based on small baseline differential SAR interferograms," *IEEE Trans. Geosci. Remote Sens.*, vol. 40, no. 11, pp. 2375–2383, Nov. 2002.
[32] D. Li, K. Z. Deng, X. X. Gao, and H. P. Niu, "Monitoring and analysis of surface subsidence in mining area based on SBAS-InSAR," *Geomatics Inf. Sci. Wuhan Univ.*, vol. 43, no. 10, pp. 1531–1537, 2018.
[33] X. M. Xing et al., "InSAR modeling and deformation prediction for salt solution mining using a novel CT-PIM function," *Remote Sens.*, vol. 14, no. 4, Feb. 2022, Art. no. 842.
[34] T. F. Zhang et al., "Time-series InSAR deformation prediction for salt mining area based on coordinate-time function (CT-PIM)—A case study of Huaian salt mine," *Nat. Remote Sens. Bull.*, pp. 1–6, Nov. 2022.
[35] A. Hyvarinen, "Fast and robust fixed-point algorithms for independent component analysis," *IEEE Trans. Neural Netw.*, vol. 10, no. 3, pp. 626–634, May 1999.
[36] A. Hyvärinen and E. Oja, "Independent component analysis: Algorithms and applications," *Neural Netw.*, vol. 13, no. 4/5, pp. 411–430, May 2000.
[37] A. Hyvärinen, "Survey on independent component analysis," *Neural Comput. Surv.*, vol. 2, pp. 94–128, Nov. 1999.
[38] W. J. Dai, B. Liu, X. L. Meng, and D. W. Huang, "Spatio-temporal modelling of dam deformation using independent component analysis," *Surv. Rev.*, vol. 46, no. 339, pp. 437–443, Nov. 2014.
[39] X. M. Xing, H.-C. Chang, L. F. Chen, J. H. Zhang, Z. H. Yuan, and Z. N. Shi, "Radar interferometry time series to investigate deformation of soft clay subgrade settlement—A case study of Lungui Highway, China," *Remote Sens.*, vol. 11, no. 4, Feb. 2019, Art. no. 429.
[40] R. F. Hanssen, *Atmospheric Heterogeneities in ERS Tandem SAR Interferometry*. Delft, The Netherlands: Delft Univ. Press, Dec. 1998, p. 137.
[41] G. D. Cheng and T. H. Wu, "Responses of permafrost to climate change and their environmental significance, Qinghai-Tibet Plateau," *J. Geophys. Res.*, vol. 122, no. F2, pp. 93–104, Jun. 2007.
[42] X. D. Liu and B. D. Chen, "Climatic warming in the Tibetan Plateau during recent decades," *Int. J. Climatol.*, vol. 20, no. 14, pp. 1729–1742, 2000.
[43] Z. L. Feng et al., "A preliminary analysis of protective effect on permafrost of typical embankment along Gonghe—Yushu Highway," *Chin. J. Rock Mechanics Eng.*, vol. 35, no. 3, pp. 638–648, Mar. 2016.
[44] X. Chen et al., "High-resolution dataset of thermokarst lakes on the Qinghai-Tibetan Plateau," *Earth Syst. Sci. Data*, vol. 2021, pp. 1–23, 2021.
[45] L. C. Huang, J. Luo, Z. J. Liu, F. J. Niu, and L. Liu, "Using deep learning to map retrogressive thaw slumps in the Beiluhe region (Tibetan Plateau) from CubeSat images," *Remote Sens. Environ.*, vol. 237, Feb. 2020, Art. no. 111534.
[46] J. Luo, F. J. Niu, Z. J. Lin, M. H. Liu, and G. A. Yin, "Recent acceleration of thaw slumping in permafrost terrain of Qinghai-Tibet Plateau: An example from the Beiluhe Region," *Geomorphology*, vol. 341, pp. 79–85, Sep. 2019.
[47] C. C. Mu et al., "Acceleration of thaw slump during 1997–2017 in the Qilian Mountains of the northern Qinghai-Tibetan plateau," *Landslides*, vol. 17, no. 5, pp. 1051–1062, 2020.
[48] Y. Chen et al., "Monitoring land surface displacement over Xuzhou (China) in 2015–2018 through PCA-based correction applied to SAR interferometry," *Remote Sens.*, vol. 11, no. 12, Jun. 2019, Art. no. 1494.
[49] D. L. Luo et al., "A review of the spatial differentiation of ground surface temperature in alpine permafrost regions," *Pratacultural Sci.*, vol. 40, no. 4, pp. 942–964, Apr. 2023.

[50] D. F. Zou et al., "A new map of permafrost distribution on the Tibetan Plateau," *The Cryosphere*, vol. 11, no. 6, pp. 2527–2542, Nov. 2017.
[51] B. Chen and J. P. Lian, "Characteristics of spatial and temporal variation of seasonal and short-term frozen soil in China in recent 50 years," *Chin. J. Atmos. Sci.*, vol. 32, no. 3, pp. 432–443, May 2008.
[52] S. Y. Tao, M. Z. Gong, J. A. He, Y. N. Hu, and J. H. Zhang, "Distribution characteristics of seasonal frozen soil in Qinghai Province and its application in lightning protection," *Meteorol. Environ. Sci.*, vol. 45, no. 5, pp. 95–104, Sep. 2022.
[53] W. Zhou, "Preamble," in *Geocryology in China*, 1st ed. Beijing, China: China Sci. Publ. & Media Ltd., 2000, pp. 1–2.
[54] T. T. Gong, B. Gao, Z. C. Ji, H. Y. Cao, and Y. L. Zhang, "Variation of active layer thickness of permafrost in the Qinghai-Tibetan Plateau based on MODIS temperature product," *Scientia Geographica Sin.*, vol. 42, no. 10, pp. 1848–1856, Oct. 2022.
[55] X. J. Ma, B. Liu, W. J. Dai, C. L. Kuang, and X. M. Xing, "Potential contributors to common mode error in array GPS displacement fields in Taiwan Island," *Remote Sens.*, vol. 13, no. 21, Oct. 2021, Art. no. 4221.
[56] P. P. Tang, "Survey on independent component analysis," Ph.D. dissertation, Chin. Acad. Sci. Univ., Beijing, China, 2014.

Xuemin Xing was born in Liaoning, China, in 1983. She received the B.S., M.S., and Ph.D. degrees in geomatics and surveying from Central South University, Changsha, China, in 2005, 2008, and 2011, respectively.

From 2016 to 2017, she was a Visiting Scholar with the Department of Environmental Sciences, Macquarie University, Sydney, NSW, Australia. She is currently an Associate Professor with the School of Traffic and Transportation Engineering, Changsha University of Science and Technology, Changsha, where she is also a Key Member of the Institute of Radar Remote Sensing Applications for Traffic Surveying and Mapping. She is also a Reviewer for three international journals and four national journals in China. She has authored more than 70 articles and ten inventions. Her research focuses on the application of time-series interferometric synthetic aperture radar technique in highway deformation monitoring, deriving spatial–temporal large-scale deformation induced by mining activities and modeling.

Jiawang Ge was born in Hunan, China, in 1999. He received the B.S. degree from the Hunan University of Science and Engineering, Yongzhou, China, in 2021. He is currently working toward the M.S. degree in surveying and mapping science and technology with the Changsha University of Science and Technology, Changsha, China.

His research interests include deformation monitoring of highways in permafrost areas and salt mines based on ICA technology.

Wei Peng was born in Hunan, China, in 1989. He received the M.S. and Ph.D. degrees in geomatics and surveying from Central South University, Changsha, China, in 2015 and 2020, respectively, and the joint Ph.D. degree in geography from Texas State University, San Marcos, TX, USA, where he was sponsored by the China Scholarship Council, from 2017 to 2018.

His research interests include InSAR surface deformation monitoring, GPS surface load deformation analysis, and highway and slope deformation modeling and analysis.

Jun Zhu was born in Changsha, China, in 1986. He received the B.S. degree from the Changsha University of Science and Technology, Changsha, in 2008, and the M.S. and Ph.D. degrees in geomatics and surveying from Central South University, Changsha, in 2011 and 2017, respectively.

He has authored more than ten papers in domestic and international academic journals, including eight papers as the first or corresponding author, and six papers in SCI/EI journals. His research interests include high-resolution interferometric data processing based on instantaneous frequency estimation and the study of desert penetration depth and physical property inversion using PolInSAR technology.

Bin Liu received the Ph.D. degree from Central South University, Changsha, China, in 2018.

He is currently Lecturer with the School of Traffic and Transportation Engineering, Changsha University of Science and Technology, Changsha. His research interests include the application of GNSS to the fields of geodesy and geophysics and the combination of GNSS and InSAR.

Jiancun Shi was born in Henan, China. She received the B.E. degree in geomatics from Qinghai University, Xining, China, in 2015, the M.S. degree in surveying science and technology from the China University of Geosciences (Beijing), Beijing, China, in 2018, and the Ph.D. degree in surveying science and technology from Central South University, Changsha, China, in 2022.

Her research interests include deformation monitoring and modeling of surface facilities in mining areas by InSAR technology.

Guanfeng Zheng was born in Guangdong, China, in 1998. He received the B.S. degree in geomatics and surveying in 2021 from the Changsha University of Science and Technology, Changsha, China, where he is currently working toward the M.S. degree in civil and hydraulic engineering.

His research interests include the application of time-series InSAR technique for deformation estimation of soft clay for urban infrastructure and InSAR deformation modeling considering repetitive stress loading.